J. Fluid Mech. (2007), *vol.* 582, *pp.* 319–340.
doi:10.1017/S0022112007005861 Printed in the United Kingdom

Wake behaviour and instability of flow through a partially blocked channel

M. D. GRIFFITH[1,2], M. C. THOMPSON[1], T. LEWEKE[2], K. HOURIGAN[1] AND W. P. ANDERSON[3]

[1]Fluids Laboratory for Aeronautical and Industrial Research (FLAIR), Department of Mechanical Engineering, Monash University, Melbourne, Victoria 3800, Australia

[2]Institut de Recherche sur les Phénomènes Hors Equilibre (IRPHE), CNRS/Universités Aix-Marseille, 49 rue Frédéric Joliot-Curie, BP 146, F-13384 Marseille Cedex 13, France

[3]School of Biomedical Sciences, Monash University, Melbourne, Victoria 3800, Australia

(Received 13 June 2006 and in revised form 21 January 2007)

The two-dimensional flow through a constricted channel is studied. A semi-circular bump is located on one side of the channel and the extent of blockage is varied by adjusting the radius of the bump. The blockage is varied between 0.05 and 0.9 of the channel width and the upstream Reynolds number between 25 and 3000. The geometry presents a simplified blockage specified by a single parameter, serving as a starting point for investigations of other more complex blockage geometries. For blockage ratios in excess of 0.4, the variation of reattachment length with Reynolds number collapses to within approximately 15 %, while at lower ratios the behaviour differs. For the constrained two-dimensional flow, various phenomena are identified, such as multiple mini-recirculations contained within the main recirculation bubble and vortex shedding at higher Reynolds numbers. The stability of the flow to three-dimensional perturbations is analysed, revealing a transition to a three-dimensional state at a critical Reynolds number which decreases with higher blockage ratios. Separation lengths and the onset and structure of three-dimensional instability observed from the geometry of blockage ratio 0.5 resemble results taken from backward-facing step investigations. The question of the underlying mechanism behind the instability being either centrifugal or elliptic in nature and operating within the initial recirculation zone is analytically tested.

1. Introduction

Interest in blockage effects on flows has increased recently, particularly due to the growing number of fluid mechanics researchers dealing with problems of bio-mechanics, such as the flow of blood through an obstructed arterial passage. In order to provide a useful base case, for the research reported here the flow past a multi-parameter geometrically complex blockage associated with an arterial stenosis is reduced to the much-simplified flow in a two-dimensional channel containing a bump defined by a single parameter. The wake of this flow has some similarities to the well-known problem of the flow past a backward-facing step, which has served as an idealized geometry to investigate flow separation (Adams & Johnston 1988; Armaly *et al.* 1983) and as a benchmark for computational fluid dynamics (Ghia, Osswald & Ghia 1989). Because of this, but bearing in mind that the movitation for this study is different, we provide a brief review of relevant literature on the flow past a backward-facing step.

Armaly *et al.* (1983) contains a detailed review of the subject, including an experimental investigation with a fixed expansion ratio (outlet to inlet section) of 1.94, and Reynolds numbers ranging through the laminar, turbulent and transitional regimes. The aspect ratio of the experimental test section was 1:36, in order to yield a nominally two-dimensional flow. With increasing Reynolds number in the laminar regime, the length of the first recirculation zone increased and was accompanied by the appearance downstream of more recirculation zones on alternating sides of the channel. The transition to turbulence was observed to begin at a Reynolds numbers of 1200 (Reynolds numbers presented in this paper are rescaled to our definition (2.1), which uses the hydraulic diameter and mean velocity in the expanded part of the channel). Prior to this, the flow was observed to become three-dimensional above $Re = 400$. The authors argued that the flow was inherently three-dimensional at this point, believing there to be an instability mechanism associated with the appearance of the secondary recirculation zone.

Numerical studies of the problem began to give more insight into the nature of the instability. Kaiktsis, Karniadakis & Orszag (1996) found the flow to be convectively unstable for Reynolds numbers in the range $700 \leqslant Re \leqslant 2500$, giving a higher Reynolds number for the appearance of three-dimensionality in the flow than that observed experimentally by Armaly *et al.* (1983). Further numerical simulations by Williams & Baker (1997) shed light on the onset of three-dimensionality. Comparing their three-dimensional simulations with two-dimensional experiments and numerical solutions, they showed that the cause of this instability was not the appearance of the secondary recirculation, but rather an interaction between a wall jet, formed at the junction of the step and endwall, and the main fluid flow.

Subsequently, Barkley, Gomes & Henderson (2002) sought to identify the intrinsic three-dimensional stability of backward-facing step flow. Through numerical stability analysis they found that the primary instability was a steady bifurcation, occurring at a critical Reynolds number of 997. This instability was located in the initial recirculation zone, possessing a "flat-roll structure", with a spanwise wavelength of 6.9 step heights. It was also shown that this instability became critical at a much lower Reynolds number than any two-dimensional bifurcation of the flow. The authors, in locating the instability within the first recirculation zone, argued that the principal mechanism could not be an interaction with the second recirculation zone, proposing instead that the mechanism was centrifugal in nature.

Other works of relevance to the subject include those of Marquillie & Ehrenstein (2003) and Gallaire, Marquillie & Ehrenstein (2006), which treat the separating boundary-layer flow over a bump. This flow bears many similarities to backward-facing step flow, with an important difference being the absence of an upper bounding wall. They found that at critical Reynolds numbers a downstream oscillation of the recirculation zone, occurring near the reattachment point, plays an important role in the absolute stability of the flow. Gallaire *et al.* (2006), continuing in a similar vein to Barkley *et al.* (2002), investigated further the possibility of the presence of a centrifugal instability acting within the recirculation zone.

Another study worthy of mention is that of Thangam & Knight (1989), which seems to be the only work available that investigates the effect of a large number of expansion ratios on backward-facing step flow. They found a strong dependence of recirculation length on step height, with a Reynolds number based on the width of the small inlet before the expansion. Nie & Armaly (2002) looked at the effect of step height on backward-facing step flow, but focused only on a narrow range of expansion ratios (1.67–2.5). They found that an increase in step height caused an increase in

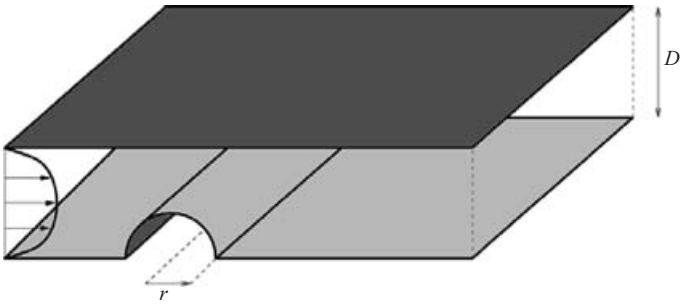

FIGURE 1. Sketch of the geometry under investigation.

reattachment length and in the general three-dimensional features of the flow. However, to maintain a constant Reynolds number across different step heights, the inlet velocity profile was varied. This kept the Reynolds number constant, but not the mass flow rate over the step. This is an issue in both the studies mentioned in this paragraph, in that the inlet conditions of the experiments and simulations are not constant over different expansion ratios. These studies, although investigating the effects of step height, do not attempt to explore with any great depth a full range of blockage effects.

The geometry studied in this paper is sketched in figure 1. It has the advantage of reducing the description of the blockage to a single parameter, and also isolating it from the calculation of the Reynolds number. While the wake flow has features in common with that of a backward-facing step, there exist several important differences. For example, the separation point is not fixed by the geometry. Also, the proposed semi-circular blockage causes a contraction of the flow upstream of the bump, in addition to the expansion and deceleration seen downstream of a backward-facing step. Furthermore, the fully developed Poiseuille profile immediately upstream of the blockage will not be present. Instead, owing to the constriction, the velocity profile at the midpoint of the blockage will be markedly skewed to one side.

The following section of this paper gives a definition of the problem and a description of the numerical methods used. In § 3 the results of the two-dimensional simulations, as well as an investigation of the stability of the system to three-dimensional disturbances, are given. Conclusions are drawn in § 4.

2. Problem definition and method

The basic geometry of the problem under examination is depicted in figure 1. The two non-dimensional parameters governing the flow behaviour are the Reynolds number Re, and the blockage ratio, defined as $b = r/D$, where r is the radius of the blockage and D the distance between the unblocked walls. The blockage ratios considered for this study lie in the range 0.05 to 0.9. The Reynolds number Re is defined as

$$Re = \frac{2D\overline{U}}{\nu}, \tag{2.1}$$

where ν is the kinematic viscosity and $2D$ corresponds to the hydraulic diameter of the channel. $\overline{U}$ is the mean flow speed in the channel. The Reynolds number used here differs from that used in many studies of the backward-facing step, which usually take the inlet channel width or the step height as the length scale. The velocity scale used in the present work is the mean velocity in the unblocked part of the channel, which would correspond to the region downstream of a backward-facing step. For this

paper, results from other studies are expressed using the Reynolds number definition (2.1); all distances and times expressed are non-dimensionalized by D and $D/\overline{U}$, respectively. The study examines laminar flows for Reynolds numbers ranging from 25 up to 3000, wherever possible. The highest Reynolds number for each blockage ratio was limited by the greater mesh resolution and computational time required to resolve the increased fluid velocity through the constriction. Hence, as the blockage ratio approached 0.9, the highest achievable Reynolds number fell accordingly. Furthermore, it is generally considered that the unblocked flow between two flat plates (plane Poiseuille flow) becomes turbulent at $Re \approx 2000$. Also germane to the issue of transition to turbulence is the potential for the blockage to act as a tripping mechanism, lowering the critical upstream Reynolds number for the appearance of turbulence. These issues of transition and three-dimensionality will be important in our considerations of instabilities in the two-dimensional base flow.

2.1. *Modelling the two-dimensional flow*

The two-dimensional flow fields were obtained from a numerical solution of the time-dependent Navier–Stokes equations, given here along with the incompressibility constraint,

$$\frac{\partial \overline{\boldsymbol{u}}}{\partial t} + \overline{\boldsymbol{u}} \cdot \nabla \overline{\boldsymbol{u}} = -\nabla \overline{p} + \nu \nabla^2 \overline{\boldsymbol{u}}, \tag{2.2}$$

$$\nabla \cdot \overline{\boldsymbol{u}} = 0, \tag{2.3}$$

where $\overline{\boldsymbol{u}} = (\overline{u}(t, x, y), \overline{v}(t, x, y))$ is the two-dimensional velocity vector and $\overline{p}$ and ν are the kinematic pressure and viscosity. The simulations were initialized with the fluid at rest and run until the flow had achieved a converged and generally steady state. Some simulations run at high Reynolds number achieved an unsteady state, with some evidence of hysteresis – these higher cases are discussed further in § 3.2. The spectral-element method used to discretize and solve the equations has been used and validated in the prediction of wake flows past rings (Sheard, Thompson & Hourigan 2003), spheres (Thompson, Leweke & Provansal 2001*a*) and circular cylinders (Thompson, Hourigan & Sheridan 1996). The method uses a three-step time-splitting procedure and has been verified to give second-order time accuracy.

2.2. *Boundary conditions*

On the blockage surface and the channel walls, no-slip conditions were imposed. At the inlet boundary, an equilibrium parabolic profile was prescribed. The functional form is given by

$$u = 6\overline{U} y(1 - y), \tag{2.4}$$

where the bottom and top walls are placed at $y = 0$ and $y = 1$, respectively. For the case of flow between flat plates, $\overline{U}$ is equal to $2/3$ of the peak velocity at the centre of the channel. At the outflow boundary, the standard zero normal velocity gradient condition was imposed.

2.3. *Stability analysis*

The stability of the two-dimensional base flow is determined by solving the linearized Navier–Stokes equations. The main aim is to determine the stability as a function of Reynolds number and spanwise wavelength, λ, or equivalently the wavenumber, $k = 2\pi/\lambda$, allowing for the possibility of both steady and time-dependent bifurcations. The same or similar techniques have been used successfully in many previous studies,

for example Barkley & Henderson (1996) and Thompson, Leweke & Williamson (2001*b*).

Starting with the two-dimensional base flow, with z and w in the spanwise direction, the velocity components and the kinematic pressure can be written as the base flow plus a perturbation:

$$\boldsymbol{u}(x, y, z, t) = \overline{\boldsymbol{u}}(x, y, t) + \boldsymbol{u}'(x, y, z, t), \tag{2.5}$$

$$p(x, y, z, t) = \overline{p}(x, y, t) + p'(x, y, z, t), \tag{2.6}$$

where $\overline{\boldsymbol{u}} = (\overline{u}, \overline{v})$ and $\overline{p}$ describe the two-dimensional base flow, and $\boldsymbol{u}' = (u', v', w')$ and p' are perturbations. Substituting these definitions into the Navier–Stokes equations, subtracting the base flow and removing nonlinear terms yields equations which describe the evolution of small disturbances:

$$\frac{\partial \boldsymbol{u}'}{\partial t} + \overline{\boldsymbol{u}} \cdot \nabla \boldsymbol{u}' + \boldsymbol{u}' \cdot \nabla \overline{\boldsymbol{u}} = -\nabla p' + \nu \nabla^2 \boldsymbol{u}', \tag{2.7}$$

$$\nabla \cdot \boldsymbol{u}' = 0. \tag{2.8}$$

Because these equations are linear and the coefficients are not a function of z, the variation in z can be constructed as a sum of complex exponentials. The coupling is such that representative modes from the series expansion, characterized by their spanwise wavelength λ, can be written in the form

$$u'(x, y, z, t) = \hat{u}(x, y, t) \sin(2\pi z/\lambda), \tag{2.9}$$

$$v'(x, y, z, t) = \hat{v}(x, y, t) \sin(2\pi z/\lambda), \tag{2.10}$$

$$w'(x, y, z, t) = \hat{w}(x, y, t) \cos(2\pi z/\lambda), \tag{2.11}$$

$$p'(x, y, z, t) = \hat{p}(x, y, t) \sin(2\pi z/\lambda). \tag{2.12}$$

Alternatively, sine and cosine terms can be interchanged to give an equivalent solution set (see for example Barkley & Henderson 1996).

These variables can then be substituted into the perturbation equations. The resultant equations describing $\hat{u}$, $\hat{v}$, $\hat{w}$ and $\hat{p}$ can be solved using the same numerical method used to solve for the base flow. Regarding the boundary conditions, the velocity and pressure perturbations are set to zero on all boundaries of the computational domain, except the outflow section, where the normal derivatives of the velocity perturbations vanish.

In this way the evolution of spanwise perturbations to the two-dimensional flow at a given wavelength λ can be determined. In general, the perturbations will either grow or decay exponentially. The time-dependence of each component of the perturbation field can be expressed as

$$\hat{\boldsymbol{\phi}}_s(x, y, t) = \exp(\sigma_s t) \hat{\boldsymbol{\phi}}_s(x, y, 0), \tag{2.13}$$

where σ_s is the growth rate, and $\hat{\boldsymbol{\phi}}_s$ denotes one of the eigenfunctions in the transverse (x, y)-plane that can be used to reconstruct the two-dimensional perturbation field. The perturbation mode will either grow or decay depending on whether its growth rate, σ_s, is positive or negative.

The growth rate is a function of the eigenmode, the spanwise wavelength and the Reynolds number. For each Reynolds number, the aim is to determine the fastest-growing or slowest-decaying mode for each wavelength. At the critical Reynolds number marking the transition to three-dimensional flow, the growth rate passes from negative to positive for a particular wavelength. In practice, the maximum

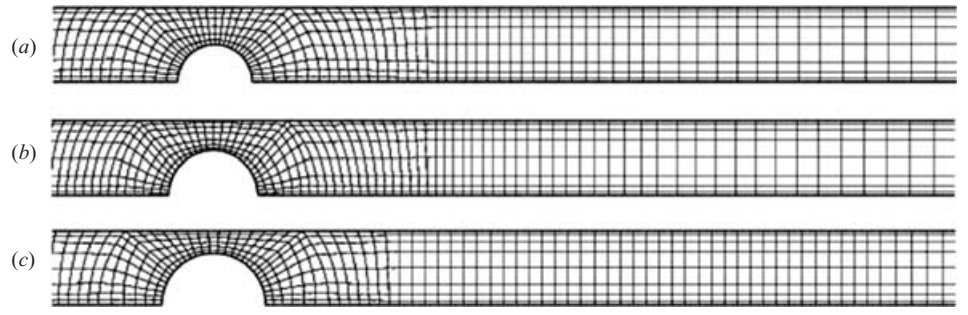

FIGURE 2. Sections of the computational meshes, from $2D$ upstream to $10D$ downstream of the blockage, showing macro-elements, used for blockage ratios (*a*) 0.5, (*b*) 0.6, (*c*) 0.7. The complete mesh extends from $6D$ upstream to $50D$ downstream in most simulations.

growth rate for each wavelength and Reynolds number pair is determined by the power method; that is, a white-noise perturbation field is integrated in time until the fastest-growing mode dominates, at which point the growth rate can be extracted.

2.4. *Mesh layout and resolution*

Ten meshes were constructed, with blockage ratios varying between 0.05 and 0.9. The same macro-element resolution was maintained across the blockage range, as far as possible. Figure 2 depicts the macro-element distribution close to the blockage sections of the grids corresponding to $b = 0.5, 0.6, 0.7$.

Each grid was constructed using the same basic layout, but adjusted for the chosen blockage ratio. In order to sufficiently resolve higher velocity gradients, the macro-element distribution was more highly concentrated near the walls of the channel and through and immediately downstream of the blockage. The resolution was decreased downstream to the outlet boundary. Each macro-element is further subdivided into $n \times n$ internal nodes, distributed according to the integration points. Functions are represented internally by $(n-1) \times (n-1)$ tensor-product Lagrangian polynomials. An advantage of the approach is the ability to set the polynomial order at run-time, allowing resolution studies to be performed more easily.

The final internal grid resolution used for most simulations was $n = 6$, or 36 nodes per element, with no marked differences observed between predictions from simulations at this resolution and those for $n = 5$. For higher blockages and Reynolds numbers, elements of order $n = 7$, comprising 49 nodes per element, were employed to properly resolve the more strongly varying regions of the flow field. For the highest Reynolds number tested at each blockage ratio, a grid resolution analysis was conducted, whereby the simulation was rerun at the next three higher values of n. Comparisons were then made based on both the length of the initial recirculation zone and on vorticity profiles at points downstream of the blockage. Over the blockage range chosen, this increase in nodal concentration produced differences of considerably less than 1 % in the recirculation length, and in the maximum difference in the vorticity profiles over the width of the channel. Small divergences from the converged vorticity profiles for these high-Reynolds-number flows only became apparent at polynomial order of $n = 5$, which generally resulted, as stated before, from inadequate resolution in areas of high flow gradients.

Further to this grid resolution check for the flow field, the convergence of the growth rate with increasing interpolant order was tested from the stability analysis for $b = 0.3$ and $Re = 2400$, $b = 0.5$ and $Re = 1200$ and $b = 0.7$ and $Re = 600$. Table 1

	$Re = 2400$, $b = 0.3$		$Re = 1200$, $b = 0.5$		$Re = 600$, $b = 0.7$	
n	L_R/r	σ	L_R/r	σ	L_R/r	σ
3	–	–	14.18	0.01615	8.942	0.1672
4	17.06	−0.001286	12.37	0.02850	8.980	0.2008
5	17.64	0.009418	12.32	0.02840	8.965	0.1928
6	17.53	0.008815	12.27	0.02834	8.960	0.1931
7	17.51	0.008554	12.28	0.02837	8.967	0.1931
8	17.52	0.008580	12.27	0.02838	8.967	0.1931
9	17.51	0.008569	12.28	0.02838	8.967	0.1931

TABLE 1. Convergence of the normalized initial recirculation length, L_R/r, and maximum growth rate, σ, across three blockage values with increasing polynomial order.

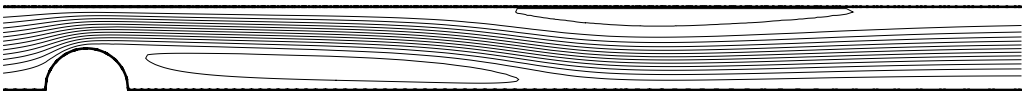

FIGURE 3. Streamlines for $b = 0.5$ and $Re = 1000$.

shows the convergence of both the growth rate for the critical wavelength from the linear stability analysis, and the length of the initial recirculation zone, L_R.

The independence of the flow predictions of the domain inlet and outlet lengths (i.e. the computational channel length upstream and downstream of the blockage) was also established. The minimum required inlet and outlet lengths were expected to increase with Reynolds number. As the flow begins to undergo its constriction upstream of the blockage, unlike the situation for the backward-facing step, care had to be taken to provide a sufficiently long inlet length; for at least a small portion of the solved flow field immediately after the computational inlet, the velocity profile should retain its symmetrical parabolic shape, before deforming to pass through the blockage. For the mesh constructed for $b = 0.5$, simulations were performed for $Re = 2000$ with inlet lengths varying between $2D$ and $10D$. The velocity profile only began to visibly skew at a little over one channel width upstream of the blockage. No differences were observed in any of the flow fields employing an inlet length of greater than $3D$. For the remainder of the study, a conservative inlet length of $6D$ was used for all blockages. The same technique was employed to determine the standard outlet length of $50D$. Hence, with the midpoint of the constriction located at $x = 0$ and the walls at $y = 0$ and $y = 1$, the inlet was located at $x = -6$ and the outlet at $x = 50$, which is also consistent with the values used in other recent numerical studies on a similar geometry featuring a constriction (Sherwin & Blackburn 2005). For blockages of $b > 0.6$, at the very highest Reynolds number, something resembling a convective instability was observed near the outflow boundary; this apparent non-physical instability disappeared if the outlet length was increased. However, importantly, no differences were observed in the flow field immediately downstream of the blockage between the flow fields obtained from grids of longer outlet length.

3. Results

The simulation geometry corresponding to $b = 0.5$ bears the most similarity to the geometry of previous work on the backward-facing step. Figure 3, showing the streamlines of the flow field for $b = 0.5$ and $Re = 1000$, gives the generic form of the

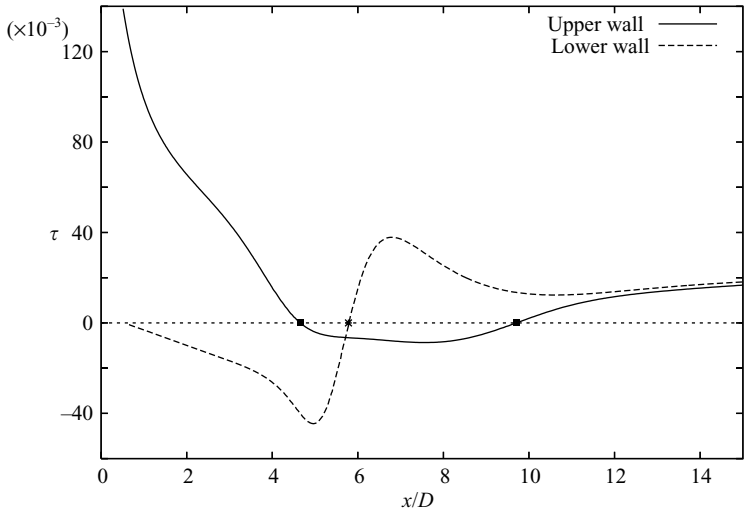

FIGURE 4. Distribution of (normalized) shear stress along the channel walls for $b = 0.5$ and $Re = 1000$. Points where the curves change sign are marked, showing the beginning and end of recirculation zones.

flow. The initial flow recirculation zone (FRZ) is formed by the sudden expansion of the flow after the constriction and the resultant adverse pressure gradient over the back half of the blockage. A further expansion near the end of the first recirculation zone causes a second separation on the opposite wall. Flows of sufficiently high Reynolds numbers can also exhibit a third separation, with each subsequent downstream recirculation attached to alternate channel walls.

3.1. *Flow recirculation length*

One parameter characterizing the flow state is the length of the first of these flow separation zones, L_R. The precise point of reattachment is best found by utilizing the wall shear stress, $\tau_{\text{wall}} = -\mu \partial u/\partial y$ (where μ is the dynamic viscosity), and finding the position on the wall where it is zero. Hence, L_R can be accurately determined by detecting where $\partial u/\partial y$ changes sign along the bottom wall. Figure 4 shows a representative example of the distribution of wall shear stress, normalized by the dynamic pressure according to $\tau = \tau_{\text{wall}}/\frac{1}{2}\rho \overline{U}^2 = -(2\nu/\overline{U}^2)(\partial u/\partial y) n_y$, where n_y describes the direction of the outward normal to the fluid. For the upper wall $n_y = 1$, and for the lower wall $n_y = -1$. Hence, in figure 4, the areas of negative τ correspond to recirculation zones, where fluid is flowing upstream in the immediate vicinity of the wall. The end of the first recirculation zone can be seen where the curve for the lower wall crosses zero, while in a similar manner the beginning and end of the recirculation zone on the upper wall are evident.

Figure 5(*a*) plots the recirculation length normalized by channel width, or L_R/D, as a function of Reynolds number. Across the blockage range, the length of the recirculation zone seems to increase approximately linearly at lower Reynolds number. It is possible that the nonlinear increase may be related to the appearance of the secondary recirculation bubble on the upper wall of the channel. The boundary for this phenomenon is depicted as the dotted line on figure 5(*a*). Below this boundary, behaviour can only be described as approximately linear, but above it, the increase in recirculation length with Reynolds number does fall away.

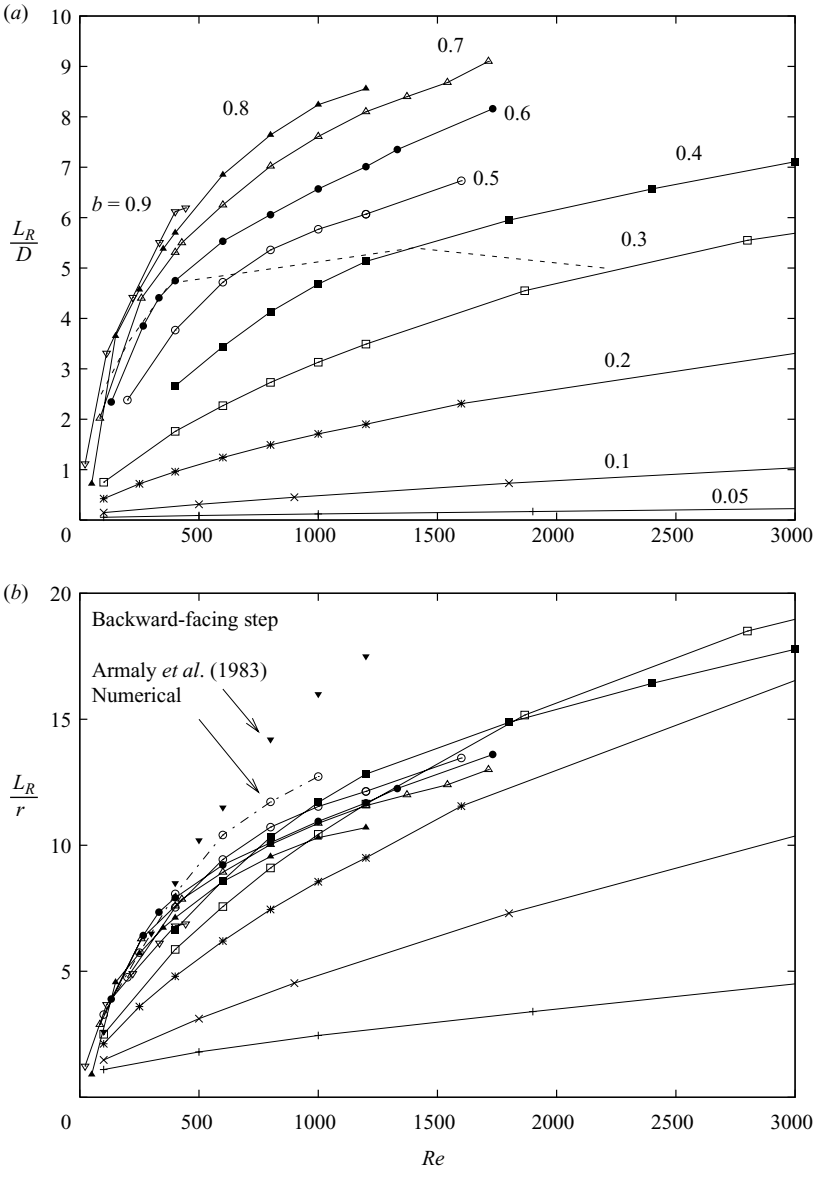

FIGURE 5. Plots of recirculation lengths against Reynolds number, Re, with L_R normalized by (*a*) channel width, D, and (*b*) blockage radius, r (point styles between the two graphs correspond). The dotted line in (*a*) shows the approximate boundary where, as Reynolds number is increased, a second recirculation zone forms on the upper wall of the channel. Also shown, on (*b*), are separation lengths for flow over a backward-facing step obtained from spectral-element simulations (open circles) and experimental measurements from Armaly *et al.* (1983) (filled triangles).

After various attempts to collapse the data, non-dimensionalization of the recirculation length by the blockage height, r, was found to yield the most useful result, as depicted in figure 5(*b*). For blockage ratios in the range $0.4 \leqslant b \leqslant 0.9$, the normalized recirculation lengths show a very similar Reynolds number dependence, with only a mild dependence on blockage ratio. For this blockage range, there is a fairly good

collapse, with the reattachment lengths at any Reynolds number matching values for other blockage ratios to within 15 % or better. Significantly reduced recirculation lengths are observed for $b < 0.3$, and in addition, the general shape of the curves is different. In particular, the variation of reattachment length with Reynolds number is much closer to linear over the Reynolds number range considered. The difference in the behaviour shown in the two regimes is probably caused by the shape of the incoming velocity profile. For small blockage ratios, the incoming velocity at the top of the blockage is much lower than the mean velocity through the channel; indeed, for $b = 0.05$ this velocity is only 28 % of the mean velocity. Hence, at low blockage ratios, the effective Reynolds number is much lower than the bulk flow Reynolds number, so that only a proportionally smaller recirculation zone is formed, as the greater part of the fluid continues on relatively unperturbed by the blockage. At higher blockage ratios, the channelling of flow through the small gap between the top of the blockage and the upper wall means that the local properties of the incoming flow profile no longer control the flow behaviour.

Predictions of the reattachment length variation for the flow over a backward-facing step are included for comparison in figure 5(*b*). These are obtained from spectral-element simulations performed by the authors, and are in agreement with accepted literature predictions using different methods (e.g. Thompson & Ferziger 1989). In addition, experimental results of Armaly *et al.* (1983) are included. Both sets of results match well with the predictions of the reattachment length for $b = 0.5$, up to $Re \approx 400$. At higher Reynolds numbers, the predicted recirculation lengths for the current geometry increase less rapidly with Reynolds number. Apart from this, there is also a divergence of the experimental and numerical results for the backward-facing step alone. As mentioned in § 1, the divergence between experimental results and purely two-dimensional simulations has been argued to be due to a three-dimensionality formed extrinsically in the experimental flows by the presence of a jet emanating from the junctions of the sidewalls with the step (Williams & Baker 1997). In view of the current focus, the more pertinent question of when the two-dimensional flow becomes intrinsically unstable to three-dimensional perturbations is addressed in § 3.3.1.

3.2. *Wake behaviour*

In addition to the initial recirculation zone, other wake parameters were recorded and other flow states identified. Figure 6 presents a parameter space map showing the boundaries for the occurrence of various phenomena in terms of blockage ratio and Reynolds number.

A second flow recirculation zone on the wall opposite the blockage was observed for $b \geqslant 0.3$ at sufficiently high Reynolds number. Similarly, a third recirculation zone appears on the bottom wall for $b \geqslant 0.6$. At $Re \gtrsim 1800$, for $b = 0.5$ and 0.6, the flow begins to shed vortices directly from the blockage, indicated on figure 6 by 'shedding'. Large vortices develop directly behind the blockage, with smaller alternating ones developing on the upper wall. Initializing these simulations from a converged steady flow solution at a lower Reynolds number, instead of from a quiescent state, shows that the onset of shedding is subcritical. In particular, by incrementing the Reynolds number in this fashion, it was found that the flow can be held steady up to $Re \approx 2600$ for $b = 0.5$. However, it is worth noting that this is well into the transitional (turbulent) Reynolds number regime for unconstricted flow between flat plates, and well past the critical Reynolds number at which the flow is unstable to three-dimensional

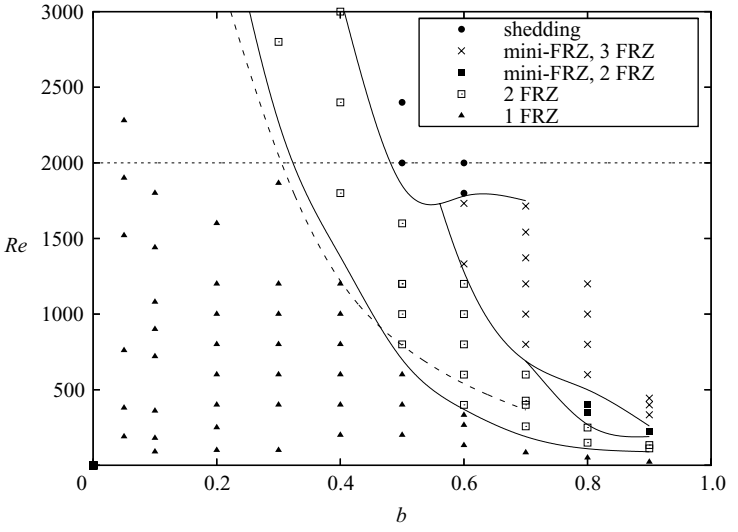

FIGURE 6. Parameter map showing the wake state as a function of Reynolds number and blockage ratio for stationary flow. The specific data points tested are plotted, while solid lines indicate the approximate boundaries between different flow states. The straight dotted line at $Re = 2000$ represents where turbulence would begin to be seen in the unconstricted flow between two flat plates. The dashed curve indicates the critical boundary for linear three-dimensional instability, derived from the stability analysis presented in § 3.3.1. The terms 1, 2 and 3 FRZ denote the number of recirculation zones present.

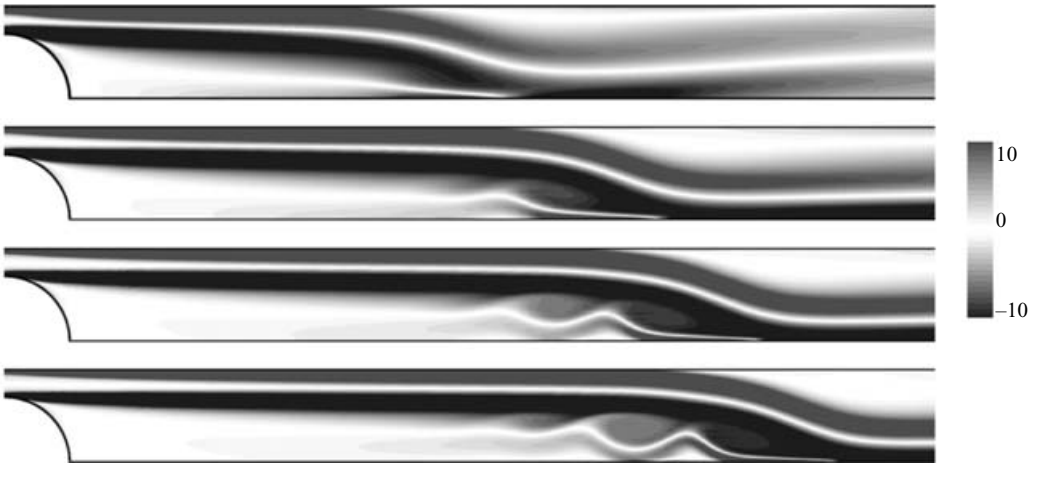

FIGURE 7. Contours of positive and negative spanwise vorticity, depicting the variation with Reynolds number of the amplitude and location of dimpling of the initial recirculation zone, at $b = 0.7$, and $Re = 400$, 800, 1200 and 1600 (top to bottom).

disturbances for flow past a backward-facing step. Hence, we have not focused further attention on this particular phenomenon.

At higher Reynolds numbers, for $b \geqslant 0.6$, the structure of the first recirculation zone begins to take on a different form. Occurrences of this steady structure are denoted by 'mini-FRZ' in figure 6, while examples are depicted in figure 7.

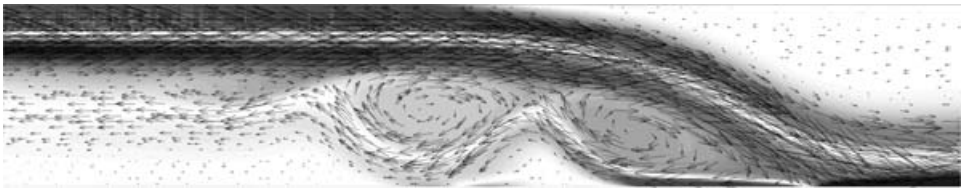

FIGURE 8. Close-up of the end of the initial FRZ for $b = 0.8$ and $Re = 1000$, showing the spanwise vorticity field overlaid with velocity vectors.

The development of these dimples in the initial recirculation zone can be seen in the vorticity fields of figure 7, with the first field being below the boundary for the occurrence of the phenomenon and the rest being above it. At $Re = 400$ the structure is not apparent, but with increasing Reynolds number, instances of these small recirculation zones grow in strength and number and occur slightly further upstream. Figure 8 is a close-up of the vorticity field of the structure, at $Re = 1000$ and $b = 0.8$, with velocity vectors overlaid. In this instance, a series of three mini-recirculations and the beginnings of a fourth are apparent. A close inspection reveals even smaller partial recirculations between those obvious in figure 8, nestled between the primary clockwise mini-vortices but attached to the bottom wall of the channel. This is somewhat reminiscent of the sequence of mini-recirculations that appear at the front of the horseshoe vortex associated with a cylinder–wall junction as the Reynolds number is increased (e.g. Thwaites 1960; Visbal 1991; Baker 1979). It should be noted that the boundary for the phenomenon shown in figure 6 denotes where the structure first becomes apparent, from observations of plots of the vorticity field.

Interestingly, we have not found any reference to such vortical structures in any of the literature on the flow past a backward-facing step. In that case, it may not occur until the Reynolds number is very much higher than is typically investigated. Considering that the critical Reynolds number for linear three-dimensional instability for a backward-facing step was found to be $Re = 997$ by Barkley *et al.* (2002), it is likely that these structures would occur for purely two-dimensional flow only above the critical Reynolds number of three-dimensional instability. This question is addressed in the following section dealing with the stability of the two-dimensional base flow.

3.3. *Three-dimensional behaviour*

3.3.1. *Instability growth rates*

Figure 9 shows converged non-dimensional growth rates corresponding to the dominant linear instability mode for $b = 0.4$, 0.5 and 0.6 as a function of Reynolds number. We initially look at the results obtained for the geometry of $b = 0.5$, which bears the most similarity to the backward-facing step, serving here as a point of reference. From figure 9(b) we see that for $b = 0.5$, the primary linear spanwise instability occurs at $Re \approx 800$, for a spanwise wavelength of ~ 5.7 blockage heights. After determining the curves for several Reynolds numbers, the critical Reynolds number Re_c, and the critical wavelength λ_c, were found by polynomial interpolation. The flow was then simulated at this Reynolds number/wavelength combination to verify the predictions. For $b = 0.5$, the critical Reynolds number is found to be $Re_c = 794$, at a wavelength of $\lambda_c = 5.7r$.

This critical Reynolds number for the transition to three-dimensionality for the geometry of $b = 0.5$ is considerably higher than the one found by Armaly *et al.*

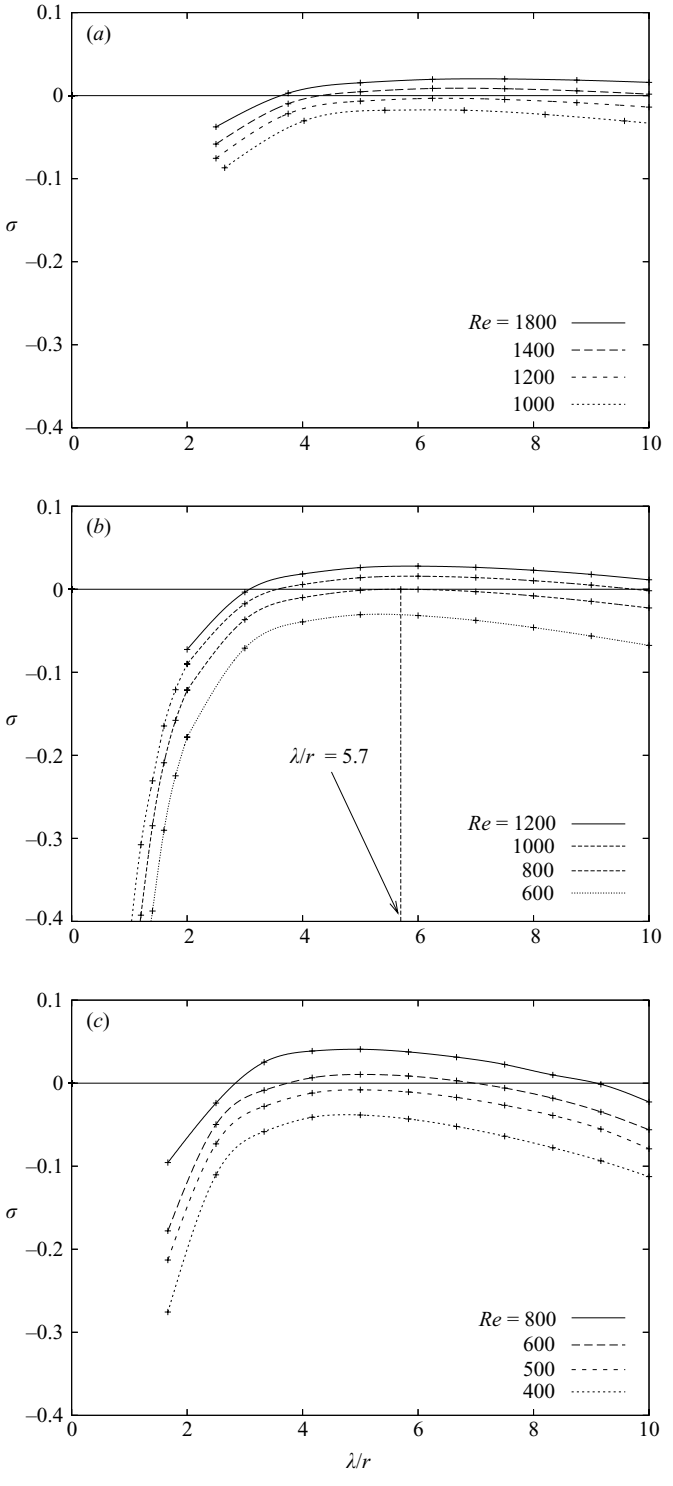

FIGURE 9. Non-dimensional growth rate as a function of wavelength, for blockage ratios of (*a*) 0.4, (*b*) 0.5 and (*c*) 0.6, at various Reynolds numbers.

(1983), and lower than that found by Barkley *et al.* (2002). As demonstrated by Williams & Baker (1997) and discussed in § 3.1, the reasons for the discrepancy with the experimental work of Armaly *et al.* (1983) probably lie in the inadequate channel width used in the experimental rig. Williams & Baker (1997) demonstrated that even in rigs of high spanwise dimension, wall jets emanating from where the step meets the sidewall penetrate into the mainstream flow, creating three-dimensional flow structures. This is similar to, but worse than, the difficulty in trying to produce a two-dimensional wake from a circular cylinder. In that case, aspect ratios need to be several hundred unless special end conditions are used. See for example Miller & Williamson (1994) or Norberg (1994).

The relatively small differences in critical Reynolds number and wavelength between the present case and the infinitely wide backward-facing step (Barkley *et al.* 2002) are not due to similar extrinsic effects, but are caused by differences in the flow geometry. The critical Reynolds number and wavelength are both approximately 20 % lower than the corresponding values for the step ($Re_c = 997$ and $\lambda_c = 6.9r$). Assuming that the nature of, and mechanism for, the instabilities in each case are analogous (see discussion below), the discrepancy in Re_c and λ_c with the backward-facing step may be related to two differences in the flow structure and topology resulting from the altered geometry. The first is the change in the velocity profile at the separation point. Over the semi-circular blockage, the velocity profile is skewed owing to the rapid constriction of the flow, with the highest velocity being closer to the bump than to the top wall. This is in contrast to the fully developed Poiseuille profile found in studies of the backward-facing step. We have not attempted to quantify this influence here. The other difference lies in the fixed point of separation present at the very edge of the backward-facing step and the mobile one in the present study. Without the sharp edge forcing the detachment of the flow, the point of separation becomes dependent on the adverse pressure gradient on the downstream half of the blockage, moving upstream with increasing Reynolds number.

The same process of determining the critical Reynolds number and wavelength was carried out for the other blockage ratios in the range $0.3 \leqslant b \leqslant 0.7$. The critical boundary is plotted on figure 6. The transition to three-dimensional flow is found to occur prior to the first appearance of the mini-recirculation zones, described in § 3.2, and well before the subcritical transition to two-dimensional vortex shedding. This is discussed further in § 3.3.3.

3.3.2. *Structure of the instability*

The structure of the dominant mode at $Re = 800$ and $b = 0.5$, for which $\lambda/r = 5.7$, is shown in figure 10. It is visualized by plotting isosurfaces of the streamwise vorticity. The repeating structure of the mode consists of two layers of opposite-signed vorticity, one almost entirely located within the recirculation zone and the other extending into the mainstream flow. The mode appears to grow around the first recirculation zone. Figure 11 shows the spanwise vorticity field of the mode, consisting of two elongated regions of opposite-signed vorticity, whose extrema are offset at a small angle. This point will prove relevant in our discussion of instability mechanisms.

The same generic mode structure is found across the blockage range tested. The structure is qualitatively similar to that of the backward-facing step found by Barkley *et al.* (2002). Figures 10 and 11 indicate that the downstream extent of the instability mode possibly scales with the length of the first recirculation zone; if this is the case, then much of the difference between the predicted critical spanwise wavelengths in the two cases can be explained by the difference in reattachment lengths at the

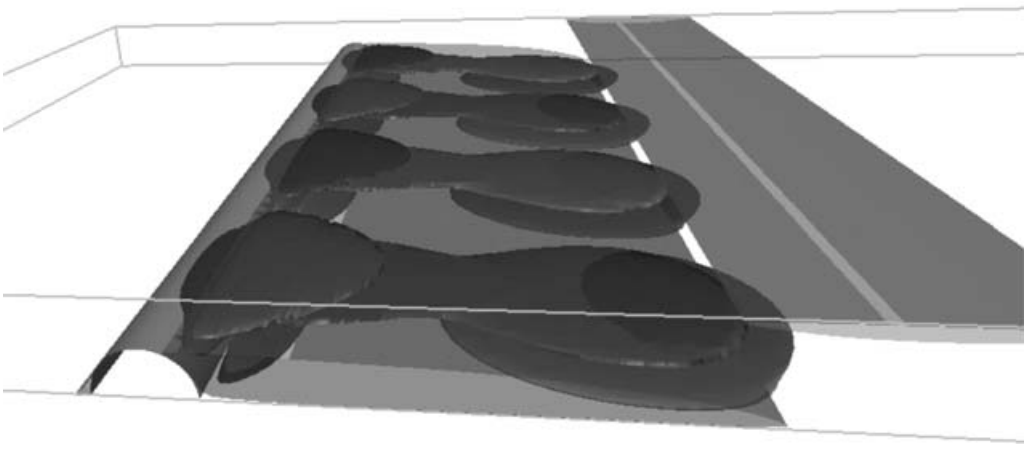

FIGURE 10. Two positive and negative iso-surfaces of the streamwise vorticity of the dominant mode, $\lambda/r = 5.7$, at $Re = 800$ and $b = 0.5$, depicted over two spanwise wavelengths. Transparent representations of the recirculation zones of the base flow are included.

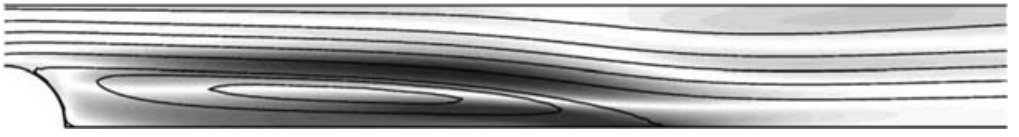

FIGURE 11. Positive and negative contours of the spanwise vorticity (colouring linear) of the critical perturbation mode, $\lambda/r = 5.7$, at $Re = 800$ and $b = 0.5$, overlaid with streamlines of the base flow.

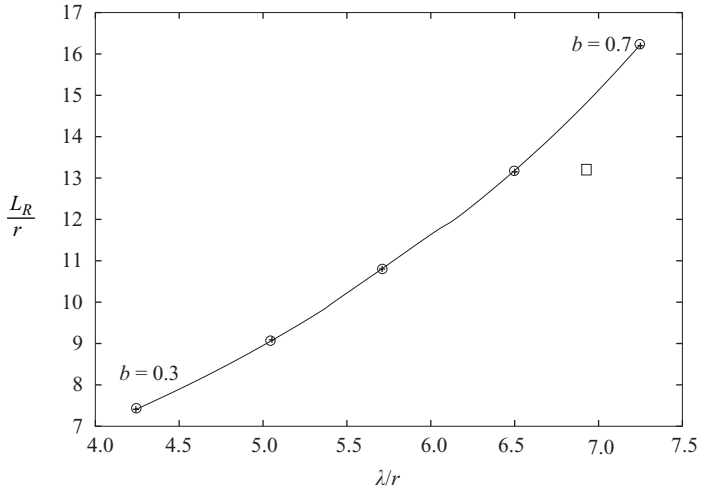

FIGURE 12. Plot of recirculation length at critical Reynolds number against critical wavelength. Both axes have been normalized by the blockage height. The square is the corresponding point for the backward-facing step taken from Barkley *et al.* (2002).

critical Reynolds number, rather than any absolute difference between the two flows. Figure 12 shows the relationship between reattachment length and critical wavelength. At the recirculation length corresponding to the critical Reynolds number for the

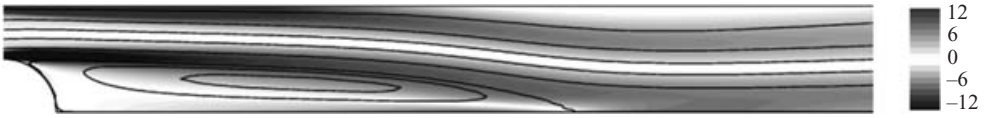

FIGURE 13. Streamlines and positive and negative contours of the spanwise vorticity of the base flow, with $b = 0.5$ and $Re = 800$.

backward-facing step, $L_R = 13.2$ (Barkley *et al.* 2002), the predicted critical wavelength is $\lambda/r \approx 6.5$, only slightly smaller than the $\lambda/r = 6.9$ obtained for the backward-facing step.

3.3.3. *Instability mechanism – centrifugal*

The strong similarity between the structure of the principal three-dimensional instability found behind the blockage and of that reported in the literature for the backward-facing step suggests taking a closer look at the previous theories on the subject of mechanisms for this instability. These have suggested that the appearance of the second recirculation zone on the upper wall, by introducing a curvature to the mainstream flow, induces a Taylor–Görtler-like instability (Ghia *et al.* 1989). In recent work using adjoint stability analysis, the instability core in similar flows has been determined to be located within the recirculation zone (Marquet *et al.* 2006). Barkley *et al.* (2002) have attributed the origins of the instability, again to a centrifugal mechanism, but this time located within the closed streamlines of the first recirculation zone.

Centrifugal instability theory, as first developed by Rayleigh (1917) for axisymmetric inviscid flows with circular streamlines, holds that a potentially unstable condition results from the existence of a decrease in angular momentum of fluid particles, as the radial distance from the centre of rotation of the flow increases, since this implies an imbalance between the radial pressure gradient and the centrifugal force acting on the fluid particles. Triggering of the instability will cause three-dimensional flow structures to form, which redistribute angular momentum between the inner and outer regions of such a vortex. The corresponding perturbations typically consist of a series of counter-rotating azimuthal vortices located in the region of decreasing circulation, and whose axial wavelength scales on the radial extent of this region. Applying this theory to irregularly curved streamlines, as in the instance found here within the initial recirculation zone, is problematic, as the flow is only locally circular with the radius of curvature varying along any one streamline. Despite this, Bayly (1988) has successfully generalized the centrifugal instability theory, making it possible to obtain predictions for any two-dimensional flow consisting of closed streamlines.

The object of this section of the paper is to give a comparison between the results of the linear stability analysis presented in § 3.3.1, which are not restricted to any specific instability type, and the stability of the flow to centrifugal instability calculated analytically through the method proposed by Bayly (1988). We focus initially on the case of $Re = 800$ and $b = 0.5$, the base flow of which is shown in figure 13.

Figure 14(a) plots the circulation within the recirculation zone, as a function of streamfunction, ψ. The centre of recirculation corresponds to $\psi = 0$. Centrifugal instability is predicted wherever there exists a decrease in circulation on moving away from the centre of rotation. As can be seen from figure 14(a), in the flow in question such a decrease exists near the edge of the recirculation zone, but the range across which it appears is extremely narrow. More quantitative predictions can be obtained

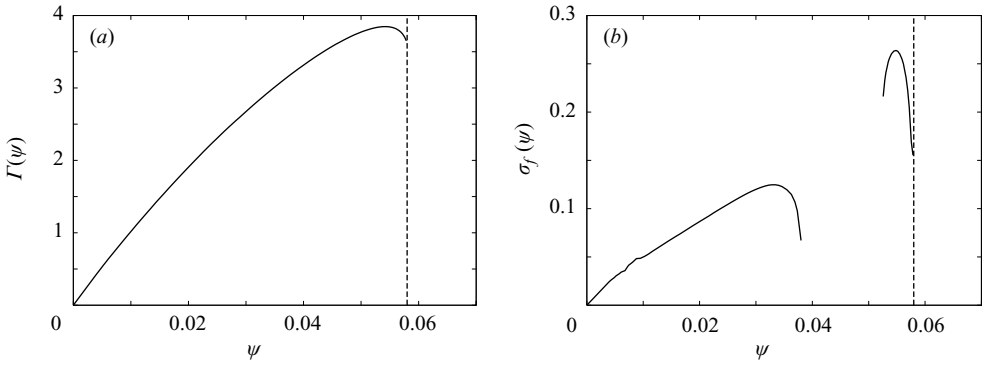

FIGURE 14. (*a*) Plot of the circulation, $\Gamma(\psi)$, within the initial recirculation zone and (*b*) plot of the real Floquet exponent, $\sigma_f(\psi)$, for $b = 0.5$ and $Re = 800$. Dotted lines show the boundary of the recirculation zone. Exponents calculated in the range $0.0384 < \psi < 0.0525$ are complex.

by first calculating the local (i.e. as a function of ψ) Floquet exponents σ_f, expressing the growth of perturbations (in the limit of short wavelengths) of fluid elements as they make one revolution on a closed streamline. Details on how to calculate these exponents from the base flow are found in Bayly (1988); the result is plotted in figure 14(*b*). The behaviour of $\sigma_f(\psi)$ in this graph matches closely that seen in Gallaire *et al.* (2006), who performed a similar analysis within the recirculation zone behind a bump on a plane wall in unbounded flow. An approximately quadratic maximum of σ_f is found at $\psi_0 \approx 0.055$, which allows the construction of centrifugal instability modes near the corresponding streamline and the calculation of their growth rates as functions of spanwise wavelength. A second peak in $\sigma_f(\psi)$ exists closer to the centre of the recirculation zone; it occurs, however, in a region of increasing outward circulation and we would therefore not expect it to play a role in any centrifugal instability. Including a viscous damping term proportional to $-\nu(2\pi/\lambda)^2$, the total viscous growth rate s can be expressed as

$$s(\lambda) = \sigma_f(\psi_0) - \frac{\lambda}{2\pi D}[-\sigma_f''(\psi_0)C(\psi_0)]^{1/2} - \frac{2A}{Re}\left(\frac{2\pi D}{\lambda}\right)^2, \tag{3.1}$$

where A is a constant of $O(1)$, and $C(\psi)$ a complex function of the two-dimensional base flow (for details see Bayly 1988). In equation (3.1), all quantities depending on ψ (i.e. σ_f, its second derivative σ_f'', and C) are evaluated for the most unstable streamline ψ_0.

Figure 15 plots the total growth rate as a function of wavelength, for $Re = 800$, 1000 and 1200, $Re = 800$ being near the critical Reynolds number determined from our earlier stability analysis. From the graph we can see that the theory predicts the flow to be stable to such an instability even up to at least $Re = 1200$. The value of the unknown coefficient A was chosen here to be 1. Other values also of $O(1)$ would obviously modify the predicted growth rate curves. Nevertheless, an important observation can be made concerning the least stable wavelength predicted, which has only a small dependence on the viscous correction. We see that any instability triggered in the recirculation zone by a centrifugal mechanism will be of wavelength $\lambda/r \approx 1$, significantly below the critical wavelength of $\lambda/r = 5.7$ determined from our numerical stability analysis, and shown in figure 9(*b*). Considering the narrow range of streamlines which exhibit a radially outward decrease in circulation, it is not

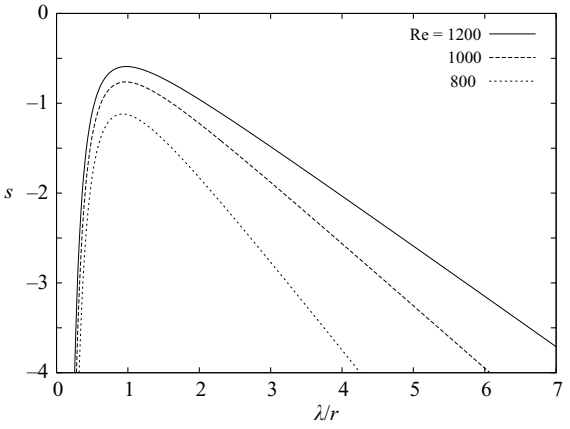

FIGURE 15. Total predicted growth rate of centrifugal instability, as a function of normalized wavelength, for $Re = 800, 1000, 1200$, according to the theory as presented in Bayly (1988).

surprising that the wavelength predicted by the centrifugal instability theory should be of a similarly small scale. Indeed, it is evident from (3.1) that the growth rate has a high dependence on σ_f'', which results in a strong damping of wavelengths significantly larger than the width of the narrow 'unstable' range of streamlines near the edge of the recirculation zone.

The analysis of this section seems to discount the possibility of the mechanism of the instability shown in figure 10 being centrifugal in nature. While the growth rates returned by the theory are well below critical, the large difference between the wavelength predicted by the theory and that determined from our numerical stability analysis lends the most weight to this argument.

3.3.4. *Instability mechanism – elliptic*

Given the strongly elongated shape of the recirculation zone in the flow under consideration, the flow's tendency to elliptic instability also merits investigation. This instability can occur in flows with elliptic streamlines, such as those found in a vortex exposed to an external strain field. The interaction of strain with normally neutral perturbation modes of the vortex can lead to a resonant amplification of these modes and thus to instability. The associated perturbations represent three-dimensional deformations of the vortex core, whose axial wavelengths scale on the transverse core size. A review of this mechanism is given by Kerswell (2002).

A first qualitative indication of elliptic instability is given by the structure of the instability mode, as seen in the plot of spanwise perturbation vorticity in figure 11. Two regions of opposite-signed vorticity are found inside the recirculation zone, indicating a shift of its centre of rotation in a spanwise-periodic way, which is characteristic of elliptic instability.

The analysis can be made more quantitative by following the same procedure as applied by Leweke & Williamson (1998) to the three-dimensional instability of circular cylinder wakes, which was based on the theoretical work on viscous elliptic instability by Landman & Saffman (1987). For elliptic flow extending to infinity, with constant streamline eccentricity β in the range $0 < \beta < 1$, the inviscid growth rate σ_i for elliptic instability, which is independent of axial/spanwise wavelength, can be

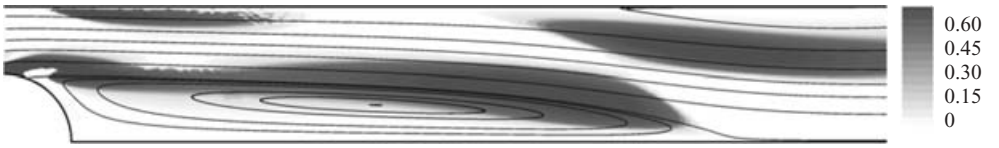

FIGURE 16. Contours of positive inviscid growth rate, σ_i, calculated locally from (3.2), along with representative streamlines of the base flow. The presence of regions of positive growth rate located within the closed streamlines suggest the possibility of elliptic stability.

approximated by

$$\sigma_i \approx \frac{9\varepsilon}{16}(1-\beta^m)^n, \tag{3.2}$$

where ε denotes the (constant and non-dimensional) strain rate of the flow, and where $m=2.811$ and $n=0.3914$ (Leweke & Williamson 1998). Despite the assumption of infinite elliptic flow with constant β made for (3.2), it is instructive to plot a local distribution of σ_i, using the relation (also derived from infinite flow) $\beta=2\varepsilon/|\omega|$, where ω is the vorticity, as function of position. The result is shown in figure 16 for the critical case with $Re=800$ and $b=0.5$, the base flow of which is shown in figure 13. The regions of strong inviscid growth rate within the mainstream flow are of no interest, as they occur upon unclosed streamlines, but a region of positive growth rate does extend into and past the centre of the recirculation zone. There is also a significant overlap between this region and the zone where the instability amplitude is strong, as observed in figure 11, which includes the recirculation zone and the adjacent shear layer.

To determine the total growth rate σ at the relatively low Reynolds numbers considered here, a viscous correction must be included. This effect was treated by Landman & Saffman (1987), and the result can be written as

$$\sigma = \sigma_i - \frac{2}{Re}\left(\frac{2\pi D}{\lambda}\right)^2 \frac{1-\beta\cos^2\theta}{(1-\beta)\cos^2\theta}. \tag{3.3}$$

In the present case, we evaluate all involved quantities at the centre of recirculation, for simplicity (this choice is partly motivated by the observations made by Eloy & Le Dizes (1999) concerning elliptic instability of a vortex with non-uniform vorticity). Here θ is the angle between the wave vector of the most unstable perturbation and the axis of rotation of the recirculation zone. It depends on the streamline eccentricity and the Reynolds number, and can in principle be obtained from figure 3 of Landman & Saffman (1987). However, in the present case, the eccentricity is always close to 1 at the centre of rotation, and without knowing beforehand the wavelength of the instability, θ cannot be determined with great accuracy. This means that unlike the case of nearly circular base-flow streamlines (i.e. low β) for which θ is always close to 60°, we are not able to predict theoretically a growth rate curve as a function of spanwise wavelength, solely based on the properties of the two-dimensional flow. We can nevertheless still perform a consistency check between the observed characteristics and the theory on elliptic instability, using additional information concerning the most unstable wavelengths obtained in the stability analysis of § 3.3.1. Indeed, if the spanwise wavelength is known, the angle θ can be calculated from the following relation between spanwise and cross-sectional length scales, which can be deduced from Landman & Saffman (1987):

$$\lambda = L\left(\frac{2}{1-\beta}\right)^{1/2}\tan\theta, \tag{3.4}$$

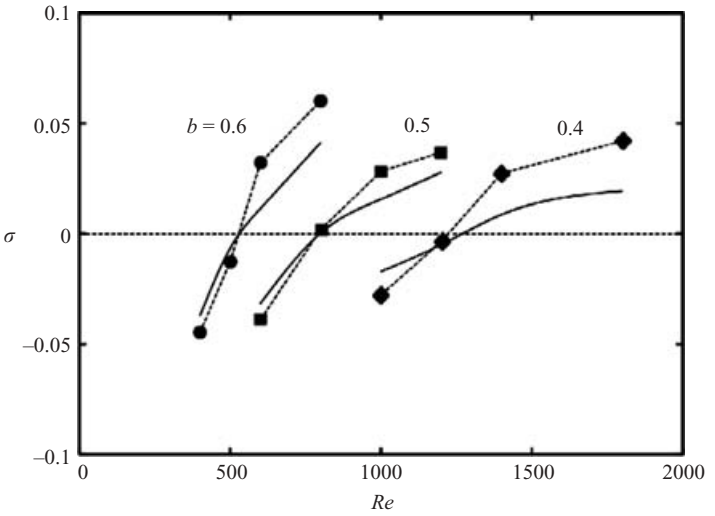

FIGURE 17. Comparison between the analytically calculated growth rates for elliptic instability, (symbols and dashed lines) and the maximum growth rates from the numerical stability analysis results of § 3.3.1 (lines), as a function of Reynolds number.

where L is a characteristic length scale of the base flow. For the present case, we choose it to be proportional to the minor axis of the recirculation zone. For elliptic instability, we would expect this length to be the constraining dimension on the development of the mode, at least more so than the other possible candidate, the major axis of the vortex. Once θ is known, the total growth rate of elliptic instability can be calculated using (3.3).

This procedure was carried out for different blockage ratios and a range of Reynolds numbers around the respective instability thresholds. Each time, the values of ε and σ_i were calculated at the centre of the recirculation zone of the base flow, the minor axis of the latter was measured, and the most unstable wavelength obtained from stability analysis. The total growth rates resulting from these parameters and the equations above derived from elliptic instability theory are plotted in figure 17, where they are compared with the ones obtained from the numerical stability analysis. A proportionality factor of 1.1 between L and the minor axis of the recirculation zone was found to give the best match, and was used for all cases.

The overall agreement between the two sets of results is quite good, given the approximations and hypotheses that had to be made in order to apply elliptic instability theory to the present high-eccentricity flow. It shows that not only the observed combinations of wavelengths and growth rates of the three-dimensional instability, but also the trends and variations with Reynolds number and blockage ratio are compatible with an elliptic instability mechanism acting in this flow.

4. Conclusions

An investigation of the flow through a partially blocked two-dimensional channel across a range of Reynolds numbers and blockage ratios has been presented. For blockage ratios $b \geqslant 0.4$, the functional dependence of the length of the initial recirculation zone on the upstream Reynolds number is insensitive to blockage ratio, if the length is normalized by blockage height. This collapse breaks down at smaller

blockage ratios. For $b < 0.3$, much shorter recirculation lengths are observed, presumably because of the lower fluid velocity in the vicinity of the blockage due to the parabolic velocity profile. In addition to the standard single recirculation region at the rear of the blockage, at higher Reynolds numbers other flow behaviours were observed, including multiple downstream recirculations attached to alternating walls, vortex shedding which appeared to be convective in nature, and sets of small positive and negative vortices at the end of the main recirculation bubble reminiscent of those that occur upstream of wall–body junctions. Most of these features occur at Reynolds number in excess of the critical Reynolds number for transition to three-dimensional flow.

The stability of the flow to three-dimensional perturbations was analysed, with the identification of a transition to three-dimensionality involving a stationary instability mode. This mode takes the form of counter-rotating cells centred around the initial recirculation zone, with the same generic structure being found between $b = 0.3$ and $b = 0.7$. The mode structure, onset Reynolds number and critical wavelength for $b = 0.5$ match well with the results taken from the literature for the flow over a backward-facing step. This is despite distinct differences in the flow profile at separation associated with the flow convergence and divergence, and the different geometry near separation. The previously proposed argument for the mechanism of the instability being centrifugal in nature was tested by means of a theoretical analysis of the flow field at the critical Reynolds number. The theory on centrifugal instabilities predicts the flow to be stable to such a mechanism and further predicts the critical wavelength, also at any other Reynolds number within our domain, to be much lower than that determined from our numerical stability analysis. Centrifugal instability therefore appears not to be the mechanism at the origin of the observed three-dimensional instability. Further analysis was carried out exploring the possibility of an elliptic instability acting in this flow. Although a straightforward theoretical prediction was not achieved, owing to the high eccentricity of the recirculation zone considered here, the observed characteristics were found to be consistent with an elliptic instability mechanism.

We would like to acknowledge the Australian Partnership for Advanced Computing (APAC) for providing the computing time which made this study possible. The authors gratefully acknowledge financial support from the Australian Research Council under both Discovery Grant DP0555897 and Linkage International LX0668992.

REFERENCES

Adams, E. W. & Johnston, J. P. 1988 Effects of the separating shear-layer on the reattachment flow structure part 2: Reattachment length and wall shear-stress. *Exps. Fluids* **6**, 493–499.

Armaly, B. F., Durst, F., Pereira, J. C. F & Schoenung, B. 1983 Experimental and theoretical investigation of backward-facing step flow. *J. Fluid Mech.* **127**, 473–496.

Baker, C. J. 1979 The laminar horseshoe vortex. *J. Fluid Mech.* **95**, 347–367.

Barkley, D., Gomes, M. G. M. & Henderson, R. D. 2002 Three-dimensional instability in flow over a backward-facing step. *J. Fluid Mech.* **473**, 167–190.

Barkley, D. & Henderson, R. D. 1996 Three-dimensional Floquet stability analysis of the wake of a circular cylinder. *J. Fluid Mech.* **322**, 215–241.

Bayly, B. J 1988 Three-dimensional centrifugal-type instabilities in inviscid two-dimensional flows. *Phys. Fluids* **31**, 56–64.

Eloy, C. & Le Dizes 1999 Three-dimensional instability of Burgers and Lamb-Oseen vortices in a strain field. *J. Fluid Mech.* **378**, 145–166.

Gallaire, F., Marquillie, M. & Ehrenstein, U. 2006 Three-dimensional transverse instabilities in detached boundary layers. *J. Fluid Mech.* To appear.

Ghia, K. N., Osswald, G. A. & Ghia, U. 1989 Analysis of incompressible massively separated viscous flows using unsteady Navier-Stokes equations. *Intl J. Numer. Meth. Fluids* **9**, 1025–1050.

Kaiktsis, L., Karniadakis, G. E. & Orszag, S. A 1996 Unsteadiness and convective instabilities in two-dimensional flow over a backward-facing step. *J. Fluid Mech.* **321**, 157–187.

Kerswell, R. R. 2002 Elliptical instability. *Annu. Rev. Fluid Mech.* **34**, 83–113.

Landman, M. J. & Saffman, P. G. 1987 The three-dimensional instability of strained vortices in a viscous fluid. *Phys. Fluids* **30**, 2339–2342.

Leweke, T. & Williamson, C. H. K. 1998 Three-dimensional instabilities in wake transition. *Eur. J. Mech.* B *Fluids* **17**, 571–586.

Marquet, O., Sipp, D., Chomaz, J.-M. & Jacquin, L. 2006 Linear dynamics of a separated flow over a rounded backward facing step: Global modes and optimal perturbations. In *6th Euromech Fluid Mechanics Conference, KTH Mechanics, Stockholm, Sweden, June 26–30, 2006*.

Marquillie, M. & Ehrenstein, U. 2003 On the onset of nonlinear oscillations in a separating boundary-layer flow. *J. Fluid Mech.* **490**, 169–188.

Miller, G. D. & Williamson, C. H. K. 1994 Control of three-dimensional phase dynamics in a cylinder wake. *Exps. Fluids* **18**, 26.

Nie, J. H. & Armaly, B. F. 2002 Three-dimensional convective flow adjacent to backward-facing step – effects of step height. *Intl J. Heat Mass Transf.* **45**, 2431–2438.

Norberg, C. 1994 An experimental investigation of the flow around a circular cylinder: influence of aspect ratio. *J. Fluid Mech.* **258**, 287.

Rayleigh, Lord 1917 On the dynamics of revolving fluids. *Proc. R. Soc. Lond.* A **93**, 148–154.

Sheard, G. S., Thompson, M. C. & Hourigan, K. 2003 From spheres to circular cylinders: Classification of bluff ring transitions and structure of bluff ring wake. *J. Fluid Mech.* **492**, 147–180.

Sherwin, S. J. & Blackburn, H. M. 2005 Three-dimensional instabilities of steady and pulsatile axisymmetric stenotic flows. *J. Fluid Mech.* **533**, 297–327.

Thangam, S. & Knight, D. D. 1989 Effect of stepheight on the separated flow past a backward facing step. *Phys. Fluids* A **1** (3), 604–606.

Thompson, M. C. & Ferziger, J. H. 1989 An adaptive multigrid method for the incompressible Navier-Stokes equations. *J. Comput. Phys.* **82**, 94–121.

Thompson, M. C., Hourigan, K. & Sheridan, J. 1996 Three-dimensional instabilities in the wake of a circular cylinder. *Expl Therm. Fluid Sci.* **12**, 190–196.

Thompson, M. C., Leweke, T. & Provansal, M. 2001*a* Kinematics and dynamics of sphere wake transition. *J. Fluids Struct.* **15**, 575–585.

Thompson, M. C., Leweke, T. & Williamson, C. H. K. 2001*b* The physical mechanism of transition in bluff body wakes. *J. Fluids Struct.* **15**, 607–616.

Thwaites, B. 1960 *Incompressible Aerodynamics*. Oxford University Press.

Visbal, M. R. 1991 On the structure of laminar juncture flows. *AIAA J.* **29**, 1273–1282.

Williams, P. T. & Baker, A. J. 1997 Numerical simulations of laminar flow over a 3d backward-facing step. *Intl J. Numer. Meth. Fluids* **24**, 1159–1183.